Cellular/Molecular

# Optogenetic Determination of Dynamic and Cell-Type-Specific Inhibitory Reversal Potentials

**Richard J. Burman,[1,2] Tara Diviney,[1] Alexandru Călin,[1] Gemma Gothard,[1] Jean-Sébastien Jouhanneau,[3,4] James F. A. Poulet,[3,4] Arjune Sen,[2] and Colin J. Akerman[1]**

[1]Department of Pharmacology, University of Oxford, Oxford OX1 3QT, United Kingdom, [2]Oxford Epilepsy Research Group, Nuffield Department of Clinical Neurosciences, University of Oxford, Oxford OX3 9DU, United Kingdom, [3]Max-Delbrück Center for Molecular Medicine in the Helmholtz Association (MDC), Berlin 13125, Germany, and [4]Neuroscience Research Center, Charité-Universitätsmedizin, Berlin 10117, Germany

**The reversal potential refers to the membrane potential at which the net current flow through a channel reverses direction. The reversal potential is determined by transmembrane ion gradients and, in turn, determines how the channel's activity will affect the membrane potential. Traditional investigation into the reversal potential of inhibitory ligand-gated ion channels ($E_{Inh}$) has relied upon the activation of endogenous receptors, such as the GABA-A receptor ($GABA_AR$). There are, however, challenges associated with activating endogenous receptors, including agonist delivery, isolating channel responses, and the effects of receptor saturation and desensitization. Here, we demonstrate the utility of using a light-gated anion channel, stGtACR2, to probe $E_{Inh}$ in the rodent brain. Using mice of both sexes, we demonstrate that the properties of this optically activated channel make it a suitable proxy for studying $GABA_AR$ receptor-mediated inhibition. We validate this agonist-independent optogenetic strategy in vitro and in vivo and further show how it can accurately capture differences in $E_{Inh}$ dynamics following manipulations of endogenous ion fluxes. This allows us to explore distinct resting $E_{Inh}$ differences across genetically defined neuronal subpopulations. Using this approach to challenge ion homeostasis mechanisms in neurons, we uncover cell-specific $E_{Inh}$ dynamics that are supported by the differential expression of endogenous ion handling mechanisms. Our findings therefore establish an effective optical strategy for revealing novel aspects of inhibitory reversal potentials and thereby expand the repertoire of optogenetics.**

*Key words:* **equilibrium potential; ion dynamics; neuronal subtypes; optogenetics; synaptic inhibition**

**Significance Statement**

**The strength of synaptic inhibition in the brain is determined, in part, by the reversal potential of the ionic currents that flow through inhibitory ligand-gated ion channels ($E_{Inh}$). Estimates of $E_{Inh}$ have traditionally used agonists to activate receptors on the cell surface, but this has limitations. Our study presents an optogenetic strategy for performing agonist-independent measurements of $E_{Inh}$ in the brain. We demonstrate the effectiveness of the approach in vitro, in vivo, and across different neuronal subtypes. Its excellent temporal control allows for measurements of $E_{Inh}$ dynamics, which reveal differences between genetically defined neuronal subpopulations. This expands the application of optogenetics and affords new opportunities to study synaptic inhibition.**

## Introduction

The reversal potential of current passing through inhibitory ligand-gated ion channels ($E_{Inh}$) affects the strength and nature of fast synaptic inhibition in the nervous system and is determined by transmembrane gradients for the ions that permeate these channels. In the brain, GABA-A receptors ($GABA_ARs$) are the principal ligand-gated ion channels that mediate fast synaptic inhibition, and these channels are predominantly permeable to chloride ($Cl^-$) ions and, to a lesser extent, bicarbonate ($HCO_3^-$) ions (Takeuchi and Takeuchi, 1967; Bormann et al., 1987; Kaila and Voipio, 1987). $E_{Inh}$ is therefore primarily determined by the equilibrium potential for $Cl^-$ ($E_{Cl}$), which results

Received July 24, 2023; revised March 31, 2024; accepted April 3, 2024.

Author contributions: R.J.B., J.F.A.P., A.S., and C.J.A. designed research; R.J.B., T.D., G.G., and J-S.M.J. performed research; R.J.B., T.D., and A.C. analyzed data; R.J.B. and C.J.A. wrote the paper.

We thank members of the Akerman Research Group for their advice and comments. We thank Joseph Raimondo (University of Cape Town) for his comments on this manuscript. The research leading to these results has received funding from the European Research Council under Grant Agreement 617670, plus BBSRC Project BB/S007938/1 and MRC Project MR/S01134X/1. This work was supported by a Shaun Johnson Memorial Scholarship sponsored by the Leverhulme Trust and Mandela Rhodes Foundation (R.J.B.). Wellcome Trust Doctoral Fellowships supported T.D. (222380/Z/21/Z), G.G. (219983/Z/19/Z), and A.C. (102364/Z/13/Z). J.F.A.P acknowledges support from the European Research Council (ERC-2015-CoG-682422) and Deutsche Forschungsgemeinschaft (DFG, FOR 2143). We thank Lex Kravitz, Luigi Petrucco, and Ethan Tyler for sharing their mouse illustrations on the SciDraw open-source platform. Some parts of the figures were created using BioRender (RRID:SCR_018361) under a license granted to R.J.B.

The authors declare no competing financial interests.

Correspondence should be addressed to Colin J. Akerman at colin.akerman@pharm.ox.ac.uk.

https://doi.org/10.1523/JNEUROSCI.1392-23.2024

from the dynamic interplay between $Cl^-$ extrusion and intrusion processes, including effluxes mediated by a potassium chloride cotransporter, KCC2 (Thompson et al., 1988; Rivera et al., 1999; Düsterwald et al., 2018) and influxes such as those mediated by $GABA_A$Rs themselves (Doyon et al., 2011; Yelhekar et al., 2017). $E_{Inh}$ is not a fixed parameter, but can vary between cells and over a range of timescales within the same cell, as a result of differences in transmembrane $Cl^-$ gradients caused by relative changes in $Cl^-$ influx and efflux (Staley and Proctor, 1999; Doyon et al., 2016b; Currin et al., 2020).

Estimates of $E_{Inh}$ have traditionally been made by activating endogenous receptors on the cell surface and measuring current flow at different membrane potentials. This involves exogenous application of an agonist (focal delivery or uncaging of GABA; Alger and Nicoll, 1979; Ilie et al., 2012; Kirmse et al., 2015) or stimulation techniques that elicit the release of a relevant endogenous agonist (electrical or optical activation of presynaptic GABA-releasing axons; Staley and Mody, 1992; Kätzel et al., 2011; Zhao et al., 2011). There are, however, limitations associated with inferring $E_{Inh}$ from endogenous receptors. Firstly, it can be difficult to be sure which receptor populations are being activated, which is problematic as $E_{Inh}$ is thought to vary between subcellular compartments (Szabadics et al., 2006; Földy et al., 2010; Ellender et al., 2014). It can be challenging to deliver the agonist to the cell of interest in intact preparations, it is often necessary to use pharmacology to isolate the receptor's response, and it is difficult to determine the receptor's own contribution to $E_{Inh}$ (Karlsson et al., 2011; Yelhekar et al., 2016). Furthermore, additional processes influence attempts to measure dynamic changes to $E_{Inh}$. Agonist application can saturate receptors, desensitization processes can alter receptor availability (Frosch et al., 1992; Jones and Westbrook, 1995), and, when stimulating axonal release, presynaptic mechanisms can alter how the agonist is delivered (Kullmann et al., 2005).

Optogenetics has provided neuroscience with an invaluable toolkit for modulating neuronal activity. Since these tools utilize light-activated ion fluxes, they also afford an untapped opportunity to examine transmembrane ion gradients. While light-activated anion pumps have been shown to alter $E_{Inh}$ (Raimondo et al., 2012), a more appropriate strategy for measuring $E_{Inh}$ would be to use a light-gated channel that passively reports transmembrane ion gradients, such as an anion channelrhodopsin (ACR; Berndt et al., 2014; Wietek et al., 2014). Within this class of opsins, Guillardia theta anion-conducting channelrhodopsin 2 (GtACR2) has excellent performance characteristics due to its large photocurrents and ion selectivity (Govorunova et al., 2015; Wiegert et al., 2017).

Here, we establish GtACR2's use as an agonist-independent strategy for probing $E_{Inh}$ in the mouse brain. This allows us to quantify the contribution of endogenous ion fluxes to $E_{Inh}$ and is leveraged to distinguish $E_{Inh}$ in different neuronal subpopulations. By using this approach to challenge ion homeostasis, we uncover cell-specific $E_{Inh}$ dynamics that are supported by the differential expression of endogenous handling mechanisms. This generates new opportunities for investigating $E_{Inh}$ using light, in a manner that is compatible with the targeting of defined cell populations and subcellular compartments.

## Materials and Methods

*Intracortical viral injections.* To selectively express the soma-targeted light-gated stGtACR2 anion channel in excitatory or inhibitory cortical neuronal subpopulations, the Cre-dependent construct pAAV_hSyn1-SIO-stGtACR2-FusionRed packaged in an adenoassociated virus 1 (AAV1) was injected into the primary somatosensory cortex (S1) of mice homozygous for either CaMKIIα-Cre (Tg(Camk2a-cre)T29-1Stl/J; The Jackson Laboratory, RRID:IMSR_JAX:018966) or PV-Cre (B6;129P2-Pvalb$^{tm1(cre)Arbr}$/J; The Jackson Laboratory, RRID:IMSR_JAX:008069). The pAAV_hSyn1-SIO-stGtACR2-FusionRed was a gift from Ofer Yizhar (Addgene plasmid #105677; http://n2t.net/addgene:105677; RRID:Addgene_105677). Mice (4 weeks, P28) were anesthetized with isoflurane (Zoetis) and placed in a stereotaxic frame (Kopf). Analgesic management included intravenous meloxicam (5 mg/kg) and buprenorphine (0.1 mg/kg) as well as intradermal Marcain (2 mg/kg) injected into the scalp. Each cornea was protected with ointment (Viscotears), and the animal's temperature was monitored throughout the procedure. The scalp was shaved (Wahl) and cleaned with a chlorhexidine-based solution (Hibiscrub). A midline incision was made that extended from the interpupillary line to the interaural line, and careful dissection was performed to expose the underlying cranium. The craniotomy (diameter <1 mm) was located over the left S1 (coordinates in relation to the bregma: 3 mm lateral, 1.2 mm posterior) and performed with a dental drill (Foredom). A beveled glass micropipette (Blaubrand IntraMARK) preloaded with undiluted virus was inserted 300 µm below the surface of the cortex. A total volume of 500 nl was injected at a rate of 33 nl/min. After every 100 nl, the micropipette was raised in 50 µm increments. Following completion of the injection, the micropipette was left in situ for an additional 5 min before it was removed. The scalp was sutured (6-0 Vicryl, Ethicon), and the animal was recovered before being returned to its home cage. Following injections, mice were maintained for at least 2 weeks.

*In utero electroporation (IUE).* Surgery was performed upon timed pregnant female C57BL/6 wild-type mice, with the day of plugging defined as embryonic Day 0.5 (E0.5). IUE was performed at E15.5 to maximize targeting of cortical pyramidal neurons in L2/3 (Tabata and Nakajima, 2001; Ellender et al., 2019). On the day of the procedure, the pregnant dam was anesthetized with isoflurane (Zoetis) and given subcutaneous analgesia (5 mg/kg meloxicam and 0.1 mg/kg buprenorphine). A midline laparotomy was performed, and the uterine horns were exposed. DNA plasmids were loaded into a micropipette made from borosilicate glass capillaries (Harvard Apparatus). The DNA plasmids consisted of Cre recombinase under the chicken β-actin (CAG) promoter, which was a gift from Connie Cepko (Addgene plasmid #13775; http://n2t.net/addgene:13775; RRID:Addgene_13775); Cre-dependent stGtACR2-FusionRed under the hSyn1 promoter, which was a gift from Ofer Yizhar (Addgene plasmid #105677; http://n2t.net/addgene:105677; RRID:Addgene_105677); and the cytosolic reporter tandem tomato (tdTomato) under the CAG promoter, which was a gift from Angelique Bordey (Addgene plasmid #83029; http://n2t.net/addgene:83029; RRID:Addgene_83029). The plasmids were combined in the following amounts: 7 µl of CAG-Cre (3 µg/µl), 7 µl of stGtACR2 (2.6 µg/µl), and 5 µl of CAG-tdTomato (3.7 µg/µl). One microliter of 0.03% fast green dye (Sigma-Aldrich) was added to make a total volume of 20 µl. For each embryo, 1.5 µl of the plasmid-containing mixture was injected intraventricularly. The anode of a 5 mm platinum Tweezertrode (BTX) was then positioned over the dorsal telencephalon external to the uterine muscle, and five pulses of 36 V (each pulse 50 ms separated by a 950 ms interval) were delivered using a pulse generator (BTX). After all embryos had been electroporated, the uterine horn was returned to the abdominal cavity, which was filled with warm sterile saline solution. The abdominal wall was closed with Vicryl sutures (Ethicon), and the skin was closed with Prolene sutures (Ethicon). Dams were closely monitored during the recovery period. Pups were screened for successful electroporation on the third postnatal day (P3), by illuminating the head with a custom-built light-emitting diode (LED, 525 nm, 30 W) to detect tdTomato fluorescence. The pups were weaned at 3 weeks of age and maintained until 6–8 weeks for experiments.

*Immunohistochemistry.* Mouse brains were fixed via transcardial perfusion of phosphate-buffered solution (PBS, 0.1 M, Sigma-Aldrich) and 4% paraformaldehyde solution (PFA, Sigma). Brains were stored for 24 h at 4°C in 4% PFA and then washed and stored in PBS containing

0.05% sodium azide (Merck). Within a week of perfusion, brains were washed in PBS and mounted onto a microtome (HM650V, Thermo Fisher Scientific) before being sectioned into 100-µm-thick coronal sections while being bathed in PBS. Thereafter, sections were washed with fresh PBS before being washed with PBS containing 0.3% Triton X-100 (Sigma-Aldrich; 0.3% PBST). Sections were then blocked in a solution containing 20% normal goat serum (NGS) in 0.3% PBST for 2 h. The sections were washed with 0.3% PBST after blocking and then incubated at 4°C with the primary antibody solution containing 10% NGS, 0.3% PBST plus the relevant antibody for Cux1 (Santa Cruz, #SC-13024, RRID: AB_2261231) or PV (Synaptic Systems, #195004, RRID:AB_2156476). After 24 h, sections were again washed in 0.3% PBST before incubation with the secondary antibody at room temperature (~25°C) for 2 h in a solution containing 5% NGS, 0.3% PBST and a fluorophore-linked secondary antibody specific for the relevant primary antibody. These included an anti-rabbit 635 for Cux1 labeling (Thermo Fisher Scientific, #A-31577, RRID:AB_2536187) and an anti-guinea pig 488 for PV labeling (Thermo Fisher Scientific, #A-11073, RRID: AB_2534117). Sections were washed in fresh PBS and mounted on slides with VectaShield (Vectorlabs). Confocal imaging was performed using a LSM 880 microscope (Zeiss) equipped with 488, 561 and 633 nm laser lines. All images were captured using a 20× water-immersion objective (W Plan-Apochromat NA 1.0) with the ZEN software (Zeiss). Image processing was performed in ImageJ software (NIH).

*Acute slice preparation.* In vitro electrophysiological experiments were performed in acute brain slices prepared from S1 of juvenile/adult mice aged 6–8 weeks, 2–3 weeks after intracerebral viral injection. Mice were first anesthetized with isoflurane (Zoetis) and decapitated. The brain was then sliced into 350 µm coronal sections using a microtome (HM650V, Thermo Fisher Scientific) in carbonated high-sucrose solution maintained at 4°C and consisting of the following (in mM): 185 mM sucrose, 1.2 $NaH_2PO_4$, 25 $NaHCO_3$, 2.5 KCl, 25 glucose, 2 $CaCl_2$ and 2 $MgCl_2$ (all Merck). The pH was adjusted to 7.3–7.4 (S20, Mettler Toledo) and the osmolarity to 300–310 mOsm (5520 Vapro, Wescor). Brain slices were recovered in an incubation chamber maintained at 37°C and containing artificial cerebrospinal fluid (aCSF) consisting of the following (in mM): 120 NaCl, 3 KCl, 1.2 $NaH_2PO_4$, 23 $NaHCO_3$, 11 D-glucose, 2 $CaCl_2$, and 2 $MgCl_2$ (pH, 7.3–7.4; mOsm, 300–310 mOsM). Slices were recovered for at least 60 min before starting electrophysiological recordings. When required, slices were transferred to a recording chamber that was continuously superfused with the bicarbonate-buffered aCSF and gassed with 95% $O_2$/5% $CO_2$ (32°C, pH 7.3–7.4, and perfusion speed of 2 ml/min).

*In vitro electrophysiological recordings.* All electrophysiological recordings were performed using an Axopatch 700 A amplifier with data acquired using the Clampex software (Molecular Devices). A HumBug noise eliminator (Digitimer) was used to remove 50 Hz noise. For in vitro whole-cell recordings, micropipettes (2–5 MΩ) with a short shaft were prepared from borosilicate glass capillaries (Harvard Apparatus) using a horizontal puller (Sutter) and filled with a $K^+$ gluconate-based internal solution, which contained the following (in mM): 126 K-Glu, 4 KCl, 4 $Na_2ATP$, 0.3 NaGTP, 10 $Na_2$-phosphocreatine, 10 HEPES, and 0.05 EGTA. For experiments in which intracellular $Cl^-$ was varied, this was achieved by adjusting the amount of K-Glu and KCl. For the 20 mM $Cl^-$ internal solution, 110 mM K-Glu and 20 mM KCl were used. For the 70 mM $Cl^-$ internal solution, 60 mM K-Glu and 70 KCl were used. All other reagents were maintained the same. For all internal solutions, pH was adjusted to 7.3 using $K^+$ hydroxide (Mettler Toledo), and osmolarity was adjusted to 287–293 mOsm (Wescor). Pipettes were back-filled with the internal solution and mounted on a micromanipulator (Sutter), positive pressure was applied, and the pipette tip was lowered under visual guidance onto the surface of a neuron's soma within the brain slice. Neurons were visualized using dot contrast and a 60× objective (LUMPlanFI/IR, NA 0.90, Olympus). To perform perforated patch-clamp recordings, the internal pipette solution was prepared immediately prior to recording by combining a high $Cl^-$ (150 mM) solution (in mM: 141 KCl, 9 NaCl, 10 HEPES) heated to 37°C with a stock solution of gramicidin A (4 mg/ml—dissolved in dimethyl sulfoxide, DMSO, Merck) to achieve a final concentration of 80 µg/ml gramicidin (Kyrozis and Reichling, 1995). The solution was then vortexed (40 s) and sonicated (20 s), before the pipette was back-filled with the gramicidin solution. Once the gigaseal had formed, perforation was monitored by observing changes in series resistance. Recording protocols were started once the series resistance had stabilized at <50 MΩ. Rupture or breakthrough of the perforation into whole-cell configuration was detected by sudden and persistent depolarization of the measured $E_{GABAAR}$, consistent with dialysis of the neuron with the high $Cl^-$ pipette solution. stGtACR2 was activated by delivering blue pulses of light via a 1,000 µm optic fiber connected to a 473 nm laser (MBL-FN-473-150mW, CNI Laser). The tip of the fiber was positioned at an image plane in the microscope, in the center of the optical axis, and directed into the 60× objective lens via a dichroic mirror. This resulted in a spot of light at the brain slice whose diameter was 65 µm, assuming zero tissue scattering. Laser intensity was controlled via a potentiometer on the laser power controller, and the timing of laser pulses was controlled via TTL pulses delivered from an analog-to-digital board (Molecular Devices), which were synchronized with the electrophysiology software. In a subset of experiments, focal GABA (100 µM, Tocris Bioscience) was applied to the soma of the recorded neuron via a micropipette attached to a picospritzer (5 psi, 10 ms, General Valve). To isolate the $GABA_AR$ response, $GABA_BRs$ were blocked by adding a selective antagonist, CGP 55845 (Cunningham and Enna, 1996), at a final concentration of 10 µM in the circulating aCSF. In a subset of experiments, KCC2 was blocked by adding a selective antagonist, VU0463271 (Delpire et al., 2012), at a final concentration of 10 µM in the circulating aCSF.

*In vivo two-photon-guided patch-clamp recordings.* In vivo-targeted patch-clamp recordings were performed based on previously published protocols (Margrie et al., 2002; Wang et al., 2016; Jouhanneau and Poulet, 2019). Mice aged 6–8 weeks that had undergone IUE were anesthetized with an intraperitoneal injection of 25% urethane (1 g/kg in sterile PBS). To counteract adverse events caused by urethane, a bolus of the anticholinergic agent, glycopyrronium bromide (0.01 mg/kg), was administered subcutaneously. Local anesthetic (Marcain 2 mg/kg) was applied intradermally in the scalp and topically in the ears prior to mounting the mouse into the head-holding apparatus (Narishige) under a surgical stereoscope (Olympus). The mouse's body temperature was maintained at 37°C using a heating mat and rectal probe. The animal's head was shaved, and an eye-protecting ointment (Viscotears) was applied to both eyes. An incision in the scalp was made using surgical scissors, and the area was expanded with blunt dissection to expose the skull. The site for the craniotomy over S1 was identified based on the area of maximum tdTomato expression, detected using a custom-built LED (525 nm, 30 W). A tissue adhesive (Vetbond) was applied to fix the surrounding scalp to the skull and to secure cranial sutures. Multiple layers of dental cement (Simplex Rapid) were applied to create a chamber on top of the skull. A 0.5 mm craniotomy was drilled over the marked region using a dental drill (Foredom). The craniotomy was submerged in the cortex buffer [containing the following (in mM): 125 NaCl, 5 KCl, 10 HEPES, 2 $MgSO_4 \cdot 7H_2O$, 2 $CaCl_2 \cdot 2H_2O$, and 10 glucose]. The bone flap and dura were removed, and the animal was then relocated onto the recording apparatus. Neurons were visualized using a custom-built two-photon microscope, which consisted of a modified confocal scan unit (Olympus FV300) coupled to a Ti:sapphire laser (Newport Spectra-Physics Mai Tai HP; 930 nm, 30 mW), and images were acquired using the FluoView software (Olympus).

In vivo patch pipettes were prepared from borosilicate glass capillaries (Harvard Apparatus) using a vertical puller (Narishige) to obtain a long shaft and a tip size of 5–8 MΩ (Jouhanneau and Poulet, 2019). Patch pipettes were filled with the same internal solutions described above, with the addition of a 15 mM Alexa Fluor 594 dye (Thermo Fisher) and mounted into an Optopatcher pipette holder (A-M Sytems) on a micromanipulator (Sutter). stGtACR2 was activated via a 50 µm diameter optic fiber (Thorlabs) embedded within the Optopatcher holder and connected to a 473 nm laser (MBL-FN-473–150mW, CNI Laser). A silver $Cl^-$ ground electrode (Multi Channel Systems) was lowered onto the surface of the nearby skull. The recording site was submerged in the cortex buffer. Pipettes with

positive pressure (200–300 mBar) were lowered onto the brain surface under 4× magnification (Plan N, NA 0.10, Olympus). The pipette was then visualized under 40× magnification (LUMPlanFI/IR NA 0.80, Olympus) and inserted into the brain to a depth of 200–300 µm, and the positive pressure was first lowered to 150–170 mBar and then to 20–30 mBar when the pipette was close to the target neuron. The Alexa dye enabled the pipette to be located under the two-photon microscope (820 nm, 50 mW), and the positive pressure released the Alexa dye into the extracellular space, revealing "shadows" of neuronal cell bodies (Kitamura et al., 2008). A neuron was approached, and when consistent changes in electrode resistance appeared and the dimple of the fluorescent dye on the neuron's membrane was visible, the positive pressure was released, and the holding potential was clamped at −70 mV in voltage-clamp mode to assist gigaseal formation. Other conventions were the same as for in vitro electrophysiological recordings.

*Determining inhibitory reversal potentials.* Voltage-clamp recordings were used to measure the reversal potential of stGtACR2 ($E_{stGtACR2}$) and the $GABA_AR$ ($E_{GABAAR}$). Step protocols involved delivering a series of voltage steps to the neuron, during which a membrane conductance was evoked by either light activation of stGtACR2 or agonist activation of $GABA_ARs$. From a holding potential of −70 mV, the voltage was stepped in 10 mV increments from −130 to −30 mV, each step lasted 500 ms, with 10 s between steps, and conductances were evoked 100 ms following the start of the steps. For analysis purposes, the membrane current was measured immediately before (i.e., "baseline" current), and then during, the evoked conductance. The two currents were then superimposed on current–voltage (IV) plots. The voltage was corrected for series resistance effects (Traynelis, 1998), by calculating the voltage drop associated with the series resistance and subtracting this from the command voltage. The point at which the two IV curves intersect reflected the reversal potential of the evoked current. In addition, the baseline current was used to infer the resting membrane potential (RMP), defined as the membrane potential at which the fitted line was equal to zero. Voltage ramp protocols were used to monitor dynamic changes in $E_{stGtACR2}$. These ramp protocols afforded frequent measurements of $E_{stGtACR2}$, which could be made before and immediately following a $Cl^-$ load. From a holding potential of −70 mV, neurons were subjected to voltage ramps under baseline conditions ("baseline ramp") or during light activation of stGtACR2. Each voltage ramp lasted 150 ms and extended from 60 mV below the holding potential to 40 mV above the holding potential (i.e., from −130 to −30 mV, at a rate of 0.7 mV/ms). For analysis purposes, the first and last 15 ms of each ramp were always excluded to avoid transient currents associated with the pipette capacitance. In some recordings, voltage-gated sodium conductances were activated as the ramp reached its most depolarized levels. Such voltage-activated conductances were as likely to occur during ramps with or without light activation and were simply excluded from the analysis by avoiding the final portion of the ramp. To isolate the stGtACR2 current associated with each voltage ramp, the baseline ramp current (i.e., without light) was subtracted from the stGtACR2-associated ramp current (i.e., with light). The isolated stGtACR2 current was then plotted on an IV curve, where the voltage was corrected for series resistance effects, as above. $E_{stGtACR2}$ was defined as the voltage at which the isolated stGtACR2 current was equal to zero, and the amplitude of the stGtACR2 conductance was determined from the gradient of the IV curve. Gramicidin-perforated patch-clamp recordings were used to measure resting $E_{Inh}$, and whole-cell patch clamp recordings were used to measure time constants of $E_{Inh}$ recovery following a $Cl^-$ load. While the pipette $Cl^-$ concentration would be expected to influence absolute $E_{Inh}$ values in the whole-cell configuration, our estimates of $E_{Inh}$ recovery dynamics assumed that any $Cl^-$ dialysis from the pipette and diffusion within the cytosol remained stable during a recording, such that time constants of $E_{Inh}$ recovery reflected transmembrane $Cl^-$ extrusion mechanisms (Deisz et al., 2011). Neurons were subjected to a $Cl^-$ load by combining a prolonged activation of stGtACR2 (1 s light pulse) and increasing the driving force for $Cl^-$ to enter the neuron by clamping the membrane potential at −20 mV.

*Single-cell RNA sequencing meta-analysis.* The levels of KCC2 (SLC12A5) RNA expression in pyramidal neurons and PV interneurons was acquired from published single-cell RNA sequencing datasets from the mouse sensory cortex (GSE60361, GSE71585, GSE60361). Each dataset was first reorganized to capture the following variables: single-cell ID, cell type for each single-cell ID, gene tested, and a matrix of the RNA expression-level measurements corresponding to each single-cell and gene tested. To normalize the data, the raw KCC2 RNA count for each neuron was divided by the total expression level of all measured genes in that neuron, and the resulting number was multiplied by the mean gene expression level across all cells within the same dataset. The resulting data was then analyzed using the ARTool to perform post hoc-aligned rank transform to measure pairwise comparisons (Wobbrock et al., 2011; Elkin et al., 2021).

*Experimental design and statistical analyses.* Most of the statistical analyses was performed using the Python SciPy library (version 3.10.9, RRID:SCR_008394). The only exception was the analysis of time constants which was performed using the one-phase decay analysis tool in the GraphPad Prism software package (v8.0.0, Dotmatics, RRID: SCR_002798). In all analyses, an alpha value ($p$-value, $p$) of <0.05 was considered significant. All data is reported as mean ± standard error of the mean (SEM). For comparison statistics, appropriate parametric and nonparametric tests were used. The statistical design for each experiment is found in the Results section and corresponding figure legends.

*Data and code availability.* Patch-clamp data was analyzed using Python 3.10 using the pyABF package (Harden, 2022). All material required to reanalyze the data is available from the corresponding authors upon reasonable request.

## Results

### Using light-gated stGtACR2 to determine inhibitory reversal potentials

A light-gated anion channel, stGtACR2, can be used to elicit inhibitory photocurrents at the cell soma (Mahn et al., 2018), and its permeability follows the lyotropic series characteristic of other anion channels such as the $GABA_AR$ (Govorunova et al., 2015; Sineshchekov et al., 2015). This suggests that these channels share a similar relative permeability to $Cl^-$ and $HCO_3^-$, which is supported by evidence that the reversal potential for GtACR2 approximates that of the $GABA_AR$ (Messier et al., 2018). This generates the opportunity to develop an optogenetic strategy for determining a neuron's inhibitory reversal potential ($E_{Inh}$; Fig. 1*A*). To establish the feasibility of determining $E_{Inh}$ optically, we expressed stGtACR2 in L2/3 pyramidal neurons of the mouse cortex. AAV encoding Cre-dependent stGtACR2 fused to a red fluorescent protein, FusionRed, was injected into S1 of CaMKIIα-Cre mice, at 4 weeks of age (Fig. 1*B*). Having confirmed that this resulted in the expression of stGtACR2-FusionRed in Cux2-expressing L2/3 pyramidal neurons (Fig. 1*C*), acute brain slices were prepared 2 weeks after AAV injections, and stGtACR2-expressing L2/3 pyramidal neurons were targeted for whole-cell voltage-clamp and patch-clamp recordings (Fig. 1*D*). To evoke stGtACR2 photocurrents, brief pulses of blue light (470 nm laser) were targeted at the recorded neuron. Meanwhile, to generate an independent estimate of $E_{Inh}$ in the same neuron, we used a traditional approach of delivering focal puffs of GABA to activate $GABA_ARs$. The agonist-evoked $GABA_AR$ currents were pharmacologically isolated by blocking $GABA_BRs$ with CGP55845 (10 µM).

The reversal potential for stGtACR2 ($E_{stGtACR2}$) was calculated by measuring the amplitude of the light-gated stGtACR2 photocurrent elicited while clamping the neuron at different holding potentials (Fig. 1*E*). This enabled us to generate separate IV plots for the baseline holding current and for the total holding current recorded during stGtACR2 activation, whose point of

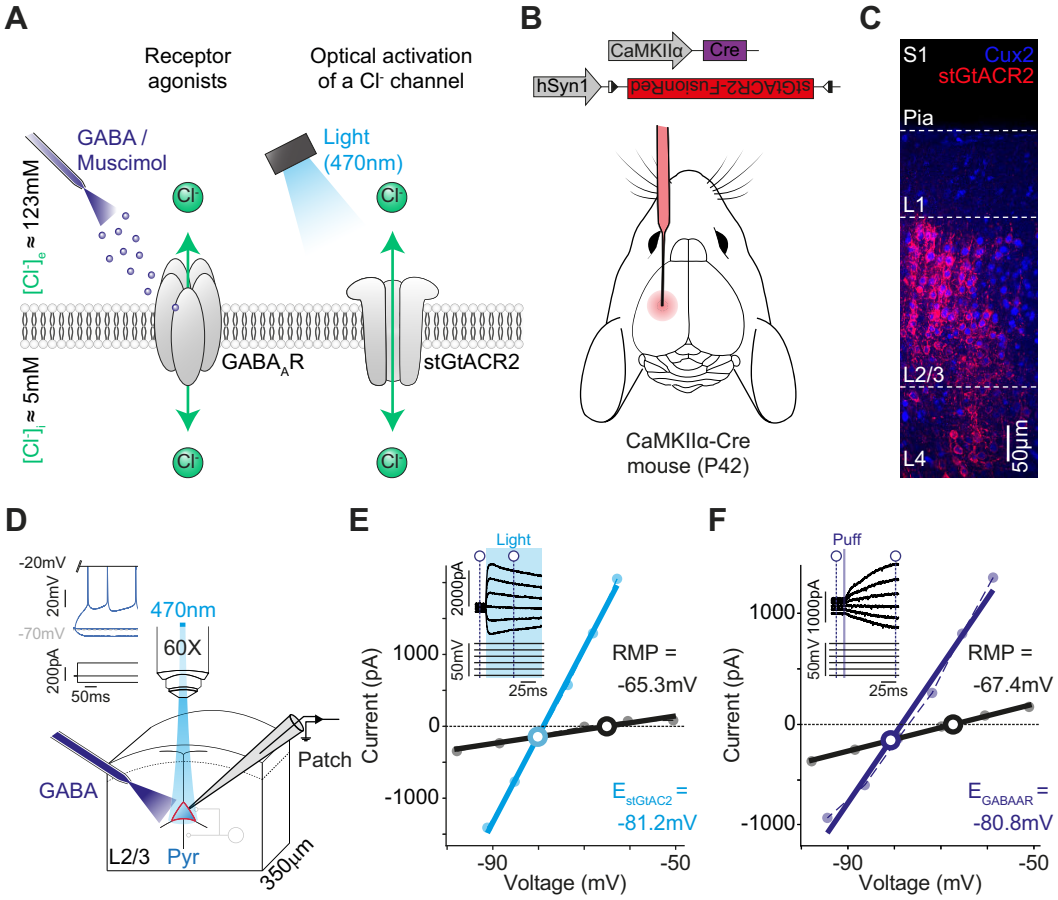


**Figure 1.** Using light-gated stGtACR2 to determine inhibitory reversal potentials. ***A***, Schematic showing transmembrane $Cl^-$ fluxes elicited by $GABA_AR$ agonist activation. An alternative, optogenetic strategy elicits transmembrane $Cl^-$ fluxes via light activation of stGtACR2. ***B***, Cre-dependent stGtACR2-FusionRed was delivered by intracerebral AAV injection into the S1 of CaMKIIα-Cre mice. ***C***, Confocal image showing stGtACR2-FusionRed expression in $Cux2^+$ L2/3 pyramidal neurons at 6 weeks of age, 2 weeks after injection. ***D***, Experimental setup in which whole-cell patch-clamp recordings were performed from stGtACR2-expressing L2/3 pyramidal neurons. stGtACR2 was activated with blue light pulses (470 nm laser) and delivered via the microscope objective. Focal applications of exogenous GABA from a separate pipette were used to activate $GABA_ARs$. Inset, current-clamp recording from an example stGtACR2-expresssing regular spiking pyramidal neuron. ***E***, IV plot from a voltage-clamp-step protocol shows the stGtACR2-induced response (cyan, 100 ms light) and baseline current (black) at different holding potentials. The reversal potential for both stGtACR2 ($E_{stGtACR2}$) and the baseline current (equivalent to the RMP) are indicated. Inset shows raw traces and indicates where baseline and stGtACR2 currents were measured (dashed vertical blue lines). ***F***, IV plot from the same neuron as in "***E***" showing the GABA-evoked response (purple) and baseline current (black) at different holding potentials, from which $E_{GABAAR}$ and RMP were determined.

intersection represents $E_{stGtACR2}$ (Fig. 1*E*). Meanwhile, an independent estimate of $E_{Inh}$ was made by measuring the amplitude of agonist-evoked $GABA_AR$ currents elicited while clamping at different holding potentials and inferring the reversal potential of current flowing through the $GABA_AR$ ($E_{GABAAR}$) in an analogous manner (Fig. 1*F*). These recordings revealed similar estimates of $E_{Inh}$ in the same neuron (Fig. 1*E*,*F*). To explore whether the relationship between $E_{stGtACR2}$ and $E_{GABAAR}$ was maintained across a wide range of intraneuronal $Cl^-$ concentrations, a series of recordings were performed using one of the three different intracellular pipette solutions (4, 20, or 70 mM $Cl^-$), such that the intraneuronal $Cl^-$ concentration was altered by dialysis. Across a population of neurons ($n = 24$ neurons from seven mice), $E_{stGtACR2}$ and $E_{GABAAR}$ were found to be significantly correlated with one another ($p < 0.0001$, Pearson's correlation coefficient; Fig. 2), supporting the idea that $E_{stGtACR2}$ can be used to estimate somatic $E_{Inh}$.

### In vivo optogenetic measurements of $E_{Inh}$

A significant advantage of determining $E_{Inh}$ optically is that it eliminates the requirement to deliver a receptor agonist, which can be technically challenging, particularly in intact tissue. To illustrate this, we asked whether stGtACR2 could be used to determine $E_{Inh}$ in vivo in the intact mouse cortex, by combining two-photon-targeted recordings with optical activation of stGtACR2. To optimize the tissue for two-photon imaging, IUE was used to express stGtACR2 in L2/3 pyramidal neurons of the S1 (Fig. 3*A*). The cytosolic fluorescent reporter protein tdTomato was coexpressed to aid in the screening of the resulting pups (see Materials and Methods) and to facilitate identification of the transfected neurons in the mature cortex (Fig. 3*B*). Once the animals had reached 6 weeks of age, they were anesthetized with urethane, and two-photon-targeted in vivo voltage-clamp and patch-clamp recordings were performed from stGtACR2-expressing L2/3 pyramidal neurons (Fig. 3*C*). Alexa 594 dye was added to the patch pipette solution to visualize the pipette under 820 nm light, while tdTomato was visualized under 930 nm light (Fig. 3*D*).

Initially, recordings performed in whole-cell configuration (Fig. 3*E*) confirmed that it was possible to combine light activation of stGtACR2 currents with voltage-step protocols at different holding potentials, thereby generating estimates of

$E_{stGtACR2}$ in vivo (Fig. 3*F*). Subsequent recordings incorporated a cation-selective perforating agent, gramicidin, into the patch pipette solution, so as to preserve the neuron's native transmembrane $Cl^-$ gradients (Fig. 3*G*). We combined our published protocol for performing gramicidin-perforated patch-clamp recordings in vivo (Alfonsa et al., 2023; Burman et al., 2023) with two-photon targeting of stGtACR2-expressing neurons. Perforation with gramicidin was confirmed by monitoring the lack of Alexa 594 dye diffusion into the neuron and from a decrease and then stabilization in series resistance following giga-seal formation (Fig. 3*G*). These recordings revealed that it was also possible to estimate resting $E_{Inh}$ under undisturbed conditions in vivo, by combining light-gated stGtACR2 currents with voltage-step protocols (Fig. 3*H*).

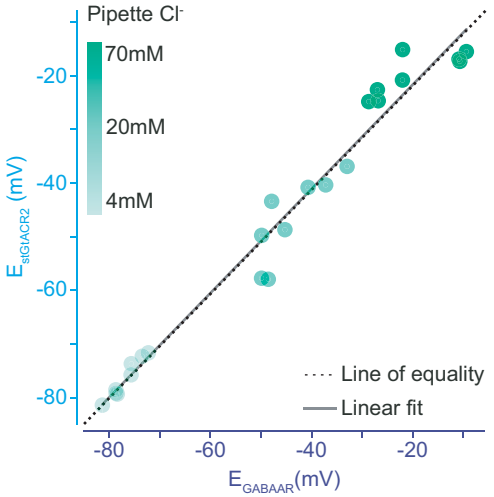


**Figure 2.** stGtACR2 reports transmembrane inhibitory reversal potentials. Across a population of neurons using a wide range of intracellular pipette $Cl^-$ concentrations, the reversal potential of stGtACR2 ($E_{stGtACR2}$) and the reversal potential of agonist-activated $GABA_ARs$ ($E_{GABAAR}$) were highly correlated (linear fitted line, black solid line, $r = 0.99$, $n = 24$ neurons from 7 mice, $p < 0.0001$, Pearson's correlation coefficient) and approached equality (dashed black line).

### Optogenetic determination of $E_{Inh}$ dynamics

Transmembrane $Cl^-$ fluxes can alter $[Cl^-]_i$, meaning that rather than being static, $E_{Inh}$ is a dynamic parameter that reflects the recent history of the cell. For example, $Cl^-$ influxes into neurons via $GABA_ARs$ can cause transient increases in $[Cl^-]_i$, which lead to depolarizing shifts in $E_{Inh}$ (Staley and Proctor, 1999; Jin et al., 2005; Raimondo et al., 2012). The rate at which $E_{Inh}$ subsequently recovers is reflective of the neuron's capacity to extrude $Cl^-$ and is an important measure of a neuron's capacity to regulate its $[Cl^-]_i$ (Deisz et al., 2011; Raimondo et al., 2012; Doyon et al., 2016a; Lanz et al., 2020; Otsu et al., 2020). An optogenetic strategy for quantifying $E_{Inh}$ dynamics has the potential to avoid confounds associated with agonist-based techniques, including controlling the amount of agonist, activating different receptor pools, and agonist-induced changes to receptors (Fig. 4*A*). Furthermore, by capitalizing on the temporal control afforded by light-gated channels, there is the potential to quantify a cell's $E_{Inh}$ dynamics and $Cl^-$ extrusion processes in real time, rather

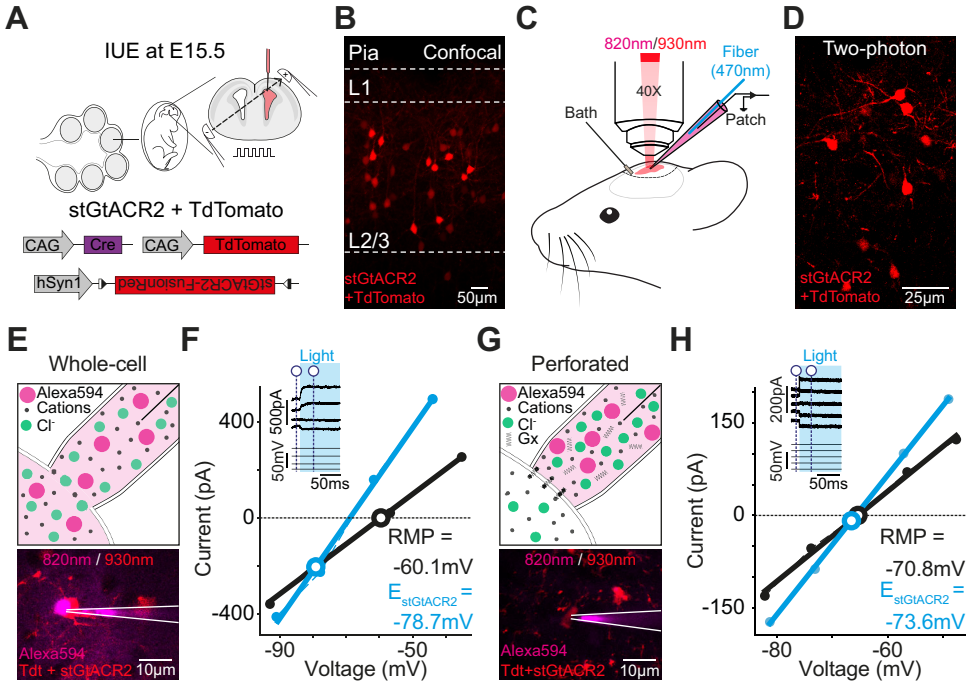


**Figure 3.** Optogenetic determination of $E_{Inh}$ in vivo. ***A***, IUE was used to coexpress stGtACR2 and tdTomato in L2/3 pyramidal neurons of the mouse S1. ***B***, Confocal image from the S1 at 6 weeks of age. tdTomato facilitated identification of expressing neurons. ***C***, Experimental setup for two-photon-targeted patch-clamp recordings. L2/3 pyramidal neurons coexpressing stGtACR2 and tdTomato were visualized at 930 nm. Patch pipettes containing Alexa 594 dye were visualized at 820 nm. Light pulses were delivered via an optic fiber inserted within the patch pipette. ***D***, In vivo two-photon image of tdTomato-expressing L2/3 pyramidal neurons. ***E***, Example image of an in vivo whole-cell patch-clamp recording (pipette solution, 4 mM $Cl^-$). The Alexa 594 dye (magenta) diffuses from the pipette (white lines) into the recorded L2/3 pyramidal neuron. ***F***, IV plot from in vivo voltage-step protocol in whole-cell mode shows stGtACR2-induced response (cyan) and baseline current (black) at different holding potentials. Inset shows raw traces and indicates where baseline and stGtACR2 currents were measured (dashed vertical blue lines). The reversal potential for stGtACR2 ($E_{stGtACR2}$) and the baseline current (RMP) are indicated. ***G***, Example image of an in vivo gramicidin (Gx)-perforated patch-clamp recording from a L2/3 pyramidal neuron. Alexa 594 dye does not enter the neuron due to the perforated status of the patch. ***H***, IV plot from in vivo gramicidin voltage-step protocol shows stGtACR2-induced response (cyan) and baseline current (black) at different holding potentials.

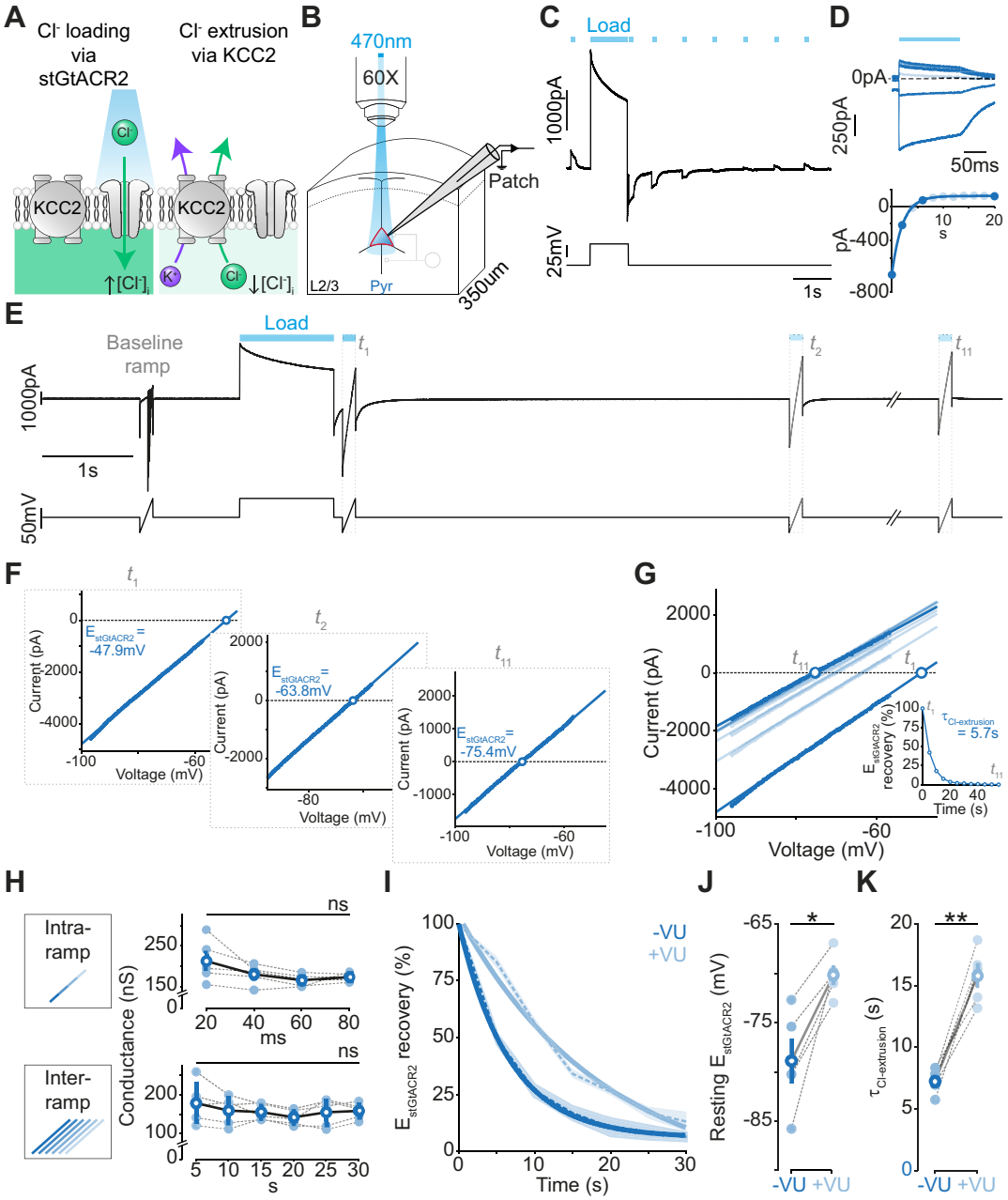


**Figure 4.** Optogenetic determination of $E_{Inh}$ dynamics. ***A***, Schematic showing intracellular $Cl^-$ being raised ("loading") during stGtACR2 activation and then extruded by KCC2. ***B***, Whole-cell patch-clamp recordings (pipette solution, 4 mM $Cl^-$) were performed from stGtACR2-expressing L2/3 pyramidal neurons in acute brain slices from the S1. ***C***, A neuron experienced a $Cl^-$ load by pairing long stGtACR2 activation (1 s light pulse, "Load") with membrane potential depolarization (to −20 mV), to increase the driving force for $Cl^-$ to enter the neuron. Following the $Cl^-$ load, delivering short light pulses (100 ms) every second revealed that the stGtACR2-current had flipped from being an outward current to transiently becoming an inward current, which then gradually returned to being an outward current. ***D***, Data from the recording in "***C***" showing the overlaid stGtACR2-current responses after the $Cl^-$ load (top) and a plot capturing the timescale of recovery of the stGtACR2-current responses (bottom). ***E***, Voltage-clamp protocol used to monitor $E_{stGtACR2}$ dynamics relative to a stGtACR2-mediated $Cl^-$ load. The traces represent the recorded current (top) and the estimated holding potential following series resistance correction (bottom). The L2/3 pyramidal neuron experienced a $Cl^-$ load by pairing long stGtACR2 activation (1 s light pulse, "Load") with membrane potential depolarization (to −20 mV). A series of voltage ramps (each 150 ms duration, labeled $t_1$–$t_{11}$) were then paired with a brief stGtACR2 activation (150 ms light pulse) to measure $E_{stGtACR2}$ dynamics at 5 s intervals over a period of 60 s. To isolate the stGtACR2 current, a baseline ramp current (without light) was subtracted from each stGtACR2-associated ramp current. ***F***, IV plots from data in "***E***" showing the isolated stGtACR2 current at $t_1$, $t_2$, and $t_{11}$. The *x*-axis intercept represents $E_{stGtACR2}$. ***G***, IV plot of isolated stGtACR2 currents from $t_1$ to $t_{11}$. Inset, plot of $E_{stGtACR2}$ recovery following the $Cl^-$ load. A single exponential fit provides the time constant of $Cl^-$ extrusion ($\tau_{Cl\text{-}extrusion}$). ***H***, The stGtACR2 conductance remained stable within each ramp (top; mean percentage change in conductance across 20 ms periods was −15.71 ± 4.01%, $p = 0.83$, one-way ANOVA) and across ramps (bottom; −10.71 ± 2.91% conductance change at intervals of 5 s, $p = 0.86$, one-way ANOVA), consistent with a modest contribution of desensitization mechanisms ($n = 5$ neurons from 3 mice). ***I***, $E_{stGtACR2}$ recovery dynamics in L2/3 pyramidal neurons under control conditions (−VU; dark cyan) and when KCC2 was blocked with the selective antagonist VU0463271 (+VU, 10 µM; light cyan). Dashed line indicates the mean, and the shaded area indicates SEM. ***J***, KCC2 block results in an increase in resting $E_{stGtACR2}$ (−VU: −78.86 ± 2.56 mV vs +VU: −70.12 ± 0.98 mV, $p = 0.01$, paired *t* test). ***K***, KCC2 block results in a slowing in $Cl^-$ extrusion (−VU: 7.29 ± 0.41 s vs +VU: 15.79 ± 0.98 s, $p = 0.001$, paired *t* test). *, $p < 0.05$. **, $p < 0.01$.

than having to infer across separate agonist applications. To investigate this possibility, we performed whole-cell patch-clamp recordings from stGtACR2-expressing L2/3 pyramidal neurons in acute brain slices (4 mM $Cl^-$ pipette concentration; Fig. 4*B*). While the whole-cell configuration would be expected to influence the neuron's absolute $E_{Inh}$, our intention was to combine the recordings with pharmacological methods to estimate the contribution that KCC2 makes to the neuron's $Cl^-$ extrusion following a $Cl^-$ load. We first asked whether stGtACR2 activation can induce an intracellular $Cl^-$ load that causes a temporary depolarizing shift in $E_{Inh}$. Adopting a protocol similar to that used by Raimondo et al. (2012), we activated stGtACR2 continuously for 1 s while depolarizing the membrane potential to increase the driving force for $Cl^-$ to enter the neuron (Fig. 4*C*). This resulted in a robust and transient $Cl^-$ load, as brief stGtACR2 photocurrents switched in polarity, such that the outward currents that were observed before the optical $Cl^-$ load became inward immediately after the $Cl^-$ load, but then decreased in amplitude, and reversed to become outward again over a period of tens of seconds (Fig. 4*C,D*).

Having established that stGtACR2 can induce $Cl^-$ loads, we designed an optogenetic protocol to quantify $E_{Inh}$ dynamics and assess the contribution of KCC2 to $Cl^-$ extrusion (Fig. 4*E*). To generate frequent measurements of $E_{stGtACR2}$ before and immediately following a $Cl^-$ load, IV plots of stGtACR2 photocurrents were produced by subtracting the current response to a control voltage ramp ("baseline ramp") from the response to the same voltage ramp delivered during stGtACR2 activation with blue light (Fig. 4*E,F*). These repeated measurements revealed that $E_{stGtACR2}$ had become more depolarized immediately following an optical $Cl^-$ load and recovered to hyperpolarized values over a period of seconds. From these real-time dynamic measurements, the neuron's $Cl^-$ extrusion capacity could be defined as the time constant of $E_{stGtACR2}$ recovery dynamics ($\tau_{Cl\text{-}extrusion}$; Fig. 4*G*), which was $7.29 \pm 0.41$ s under control conditions ($n = 5$ neurons from three mice). We noted that the stGtACR2 conductance was stable both within each ramp and between ramps, consistent with low levels of stGtACR2 desensitization during these measurements (Fig. 4*H*). To determine the contribution of KCC2 to these $E_{Cl}$ dynamics, we added the KCC2-specifc antagonist VU0463271 ("VU") to the perfusate and repeated the protocol (Fig. 4*I*). In addition to an effect upon resting $E_{stGtACR2}$ values (Fig. 4*J*), blocking KCC2 resulted in a slowing in the rate of $E_{stGtACR2}$ recovery dynamics, such that the $\tau_{Cl\text{-}extrusion}$ more than doubled (Fig. 4*K*). Thus, our measurements of $E_{stGtACR2}$ provide an effective readout of $E_{Inh}$ dynamics while avoiding the confounders associated with agonist-based techniques.

### Optogenetic discrimination of neuron-specific differences in $E_{Inh}$

Optimal methods for determining $E_{Inh}$ should be able to distinguish cells that differ in their ion handling mechanisms. Several reports have suggested that parvalbumin (PV)-expressing fast-spiking interneurons and pyramidal neurons exhibit differences in their $Cl^-$ homeostasis, although there has been no consensus on the relative contribution that cation $Cl^-$ cotransporters (CCCs) make in these neuron types (Verheugen et al., 1999; Martina et al., 2001; Banke and McBain, 2006; Vida et al., 2006; Sauer and Bartos, 2010; Otsu et al., 2020). We took advantage of the Cre-lox recombination system and our optogenetic approach to investigate potential differences in resting $E_{Inh}$ and $E_{Inh}$ dynamics between PV interneurons and pyramidal neurons. We performed intracortical viral injections of Cre-dependent stGtACR2-FusionRed into S1 of PV-Cre transgenic mice (Fig. 5*A*). Using this approach, we were able to restrict stGtACR2 expression to PV interneurons (Fig. 5*B*), which could then be targeted for gramicidin-perforated patch-clamp recordings, to preserve native transmembrane $Cl^-$ gradients (Fig. 5*C*). Equivalent recordings were performed from pyramidal neurons following stGtACR2 expression in the S1 of CaMKIIα-Cre mice (as in Fig. 1*B*).

Voltage-step protocols were used to compare resting $E_{stGtACR2}$ in L2/3 PV interneurons and pyramidal neurons, before and after pharmacologically blocking KCC2 with VU (Fig. 5*D*). This revealed a more depolarized resting $E_{stGtACR2}$ in PV interneurons than pyramidal neurons (Fig. 5*E*), confirming that optogenetic $E_{Inh}$ measurements can distinguish between neuron types. The PV interneurons also had more depolarized RMPs than the pyramidal neurons (Fig. 5*F*), and, consequently, there was no difference in the driving force for stGtACR2 ($E_{stGtACR2} - RMP$) between the two cell types at rest (Fig. 5*G*). VU application caused a depolarizing shift in the resting $E_{stGtACR2}$ of PV interneurons and pyramidal neurons, revealing that KCC2-mediated extrusion contributes to resting $E_{Inh}$ in both neuron types (Fig. 5*D*). The VU-associated shifts in resting $E_{stGtACR2}$ were comparable for the two neuron types, suggesting that the neuron types could not be distinguished in terms of KCC2's contribution (Fig. 5*H*).

### Optogenetic $E_{Inh}$ dynamics reveal neuron-specific KCC2-mediated extrusion

It has been suggested that KCC2 activity is better revealed when a neuron is subjected to a $Cl^-$ load, as this challenges the neuron's capacity to extrude $Cl^-$ (Jarolimek et al., 1999; Payne et al., 2003; Deisz et al., 2011). To test if optogenetic $E_{Inh}$ measurements can be used to resolve more subtle cell-type differences in KCC2 activity, we used whole-cell patch-clamp recordings to quantify $E_{stGtACR2}$ dynamics in L2/3 PV interneurons and compared these with equivalent recordings in pyramidal neurons (Fig. 6*A*). As we had observed in pyramidal neurons (Fig. 4), $E_{stGtACR2}$ in PV interneurons exhibited depolarized values immediately following a stGtACR2-mediated $Cl^-$ load and then gradually returned to hyperpolarized values over a period of seconds (Fig. 6*B,C*). The amplitude of the PV interneuron stGtACR2 conductance was stable within each ramp, and between ramps, consistent with a modest contribution of desensitization mechanisms during the estimates of PV interneuron $E_{stGtACR2}$ dynamics (Fig. 6*D*). Each PV interneuron's $Cl^-$ extrusion capacity was therefore defined from the time constant of $E_{stGtACR2}$ recovery dynamics ($\tau_{Cl\text{-}extrusion}$; Fig. 6*C*), which was shown at the population level to slow when KCC2 was blocked with VU (Fig. 6*E*).

A direct comparison of these dynamics across cell types revealed clear differences between PV interneurons and pyramidal neurons (Fig. 6*F–H*). Firstly, the rate of $E_{stGtACR2}$ recovery was slower in PV interneurons than in pyramidal neurons (Fig. 6*F*). This cell-type difference was abolished when KCC2 was blocked with VU (Fig. 6*G*), and a direct comparison of KCC2's contribution with $\tau_{Cl\text{-}extrusion}$ revealed that KCC2 makes a smaller contribution to $Cl^-$ extrusion mechanisms in PV interneurons (Fig. 6*H*). To corroborate these functional observations, we performed a meta-analysis of single-cell RNA sequencing studies that have distinguished pyramidal neurons and PV interneurons in the mouse sensory cortex (Zeisel et al., 2015; Tasic et al., 2016, 2018; Fig. 6*I*). After normalizing for total gene expression per cell, we observed that the expression levels of KCC2 were lower in PV interneurons compared with pyramidal neurons. This difference was evident in two independent large-scale

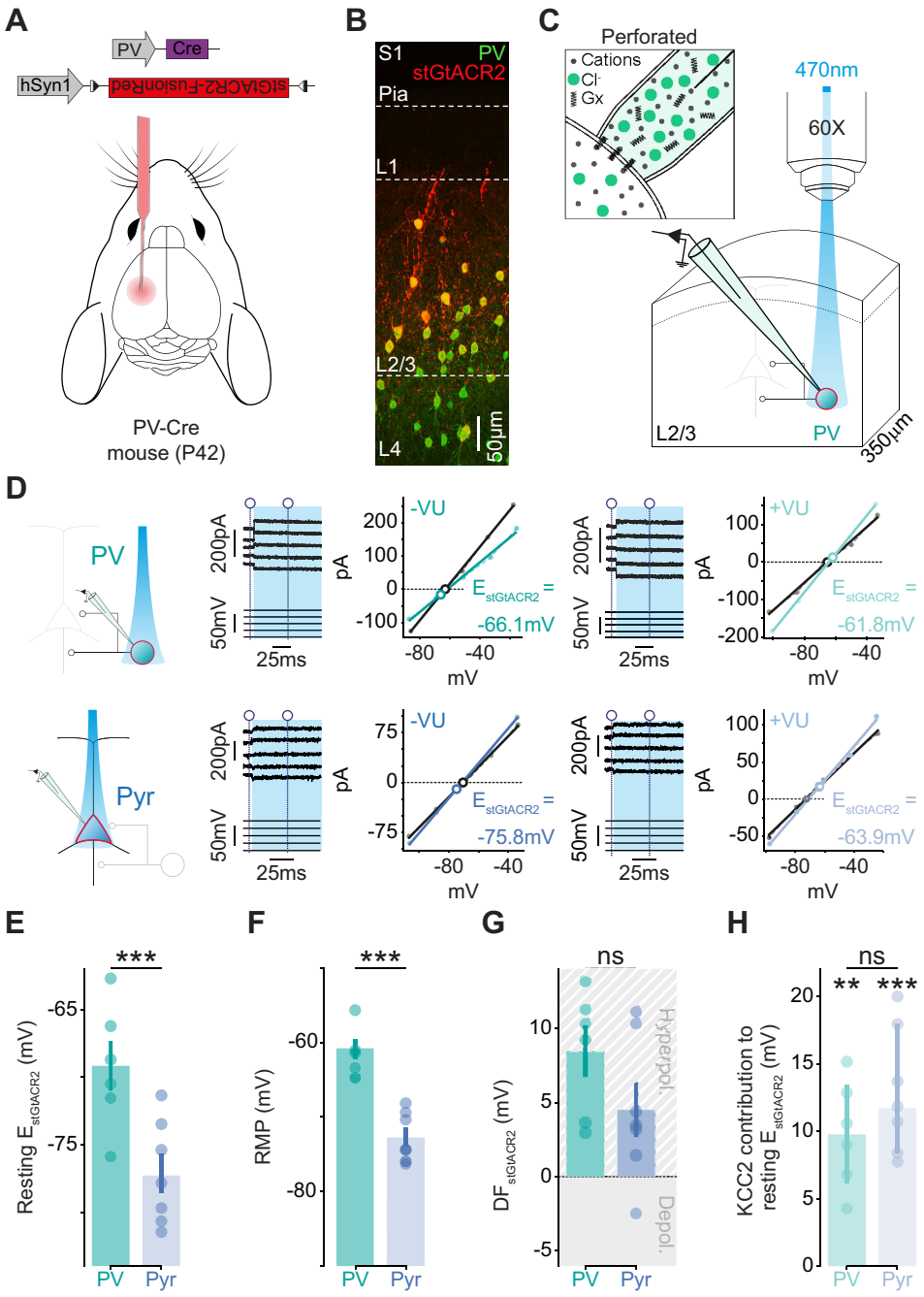


**Figure 5.** Optogenetic discrimination of neuron-specific differences in resting $E_{Inh}$. ***A***, Mice expressing Cre recombinase in PV interneurons received S1 injections of Cre-dependent stGtACR2-FusionRed AAV. ***B***, Confocal image showing selective expression of stGtACR2-FusionRed (red) in L2/3 immunohistochemically confirmed PV interneurons (green). ***C***, Setup in which gramicidin (Gx)-perforated patch-clamp recordings were performed from stGtACR2-expressing PV interneurons. ***D***, Resting $E_{stGtACR2}$ was measured in PV interneurons (turquoise, top) and pyramidal neurons (blue, bottom) using a voltage-clamp-step protocol. The resulting IV plots indicate resting $E_{stGtACR2}$ under control conditions (−VU; darker) and when KCC2 was blocked with VU0463271 (+VU; lighter). ***E***, Resting $E_{stGtACR2}$ was more depolarized in PV interneurons compared with pyramidal neurons (PV: −69.16 ± 4.54 mV, $n = 6$ neurons from 3 mice vs Pyr: −77.12 ± 3.83 mV, $n = 7$ neurons from 5 mice, $p = 0.006$, unpaired $t$ test). Pyramidal neuron data replotted from Figure 4. ***F***, The RMP of PV interneurons was more depolarized than the RMP of pyramidal neurons (PV: −60.74 ± 1.26 mV vs Pyr: −72.68 ± 1.31 mV, $p < 0.0001$, unpaired $t$ test). ***G***, The driving force for stGtACR2 ($DF_{stGtACR2} = RMP - E_{stGtACR2}$) was not significantly different between the cell types (PV: 8.42 ± 1.71 mV vs Pyr: 4.50 ± 1.82 mV, $p = 0.15$, unpaired $t$ test). ***H***, PV interneurons and pyramidal neurons both exhibited a significant contribution of KCC2 to resting $E_{stGtACR2}$ (PV: 9.79 ± 1.62 mV, $n = 6$ neurons from 3 mice, $p = 0.002$, one-sample $t$ test; Pyr: 12.92 ± 1.76 mV, $n = 7$ neurons from 5 mice, $p = 0.0003$, one-sample $t$ test), and there was no detectable difference in the contribution of KCC2 to resting $E_{stGtACR2}$ in the two neuronal populations ($p = 0.23$, unpaired $t$ test). **, $p < 0.01$; ***, $p < 0.001$; ns, not significant.

datasets from the primary visual cortex (V1), and a similar trend was also observed in a dataset from the S1 that comprised a smaller number of PV interneurons. Taken together, these results support the conclusion that optogenetic estimates of $E_{Inh}$ dynamics can reveal functionally relevant differences in neuron-specific $Cl^-$ extrusion mechanisms.

## Discussion

Here, we describe an optogenetic strategy for probing resting and dynamic $E_{Inh}$ in a cell-specific and subcellular-targeted manner. We demonstrate that this meets important prerequisites for studying inhibitory reversal potentials while offering advantages over traditional agonist-based methods. The strategy is validated

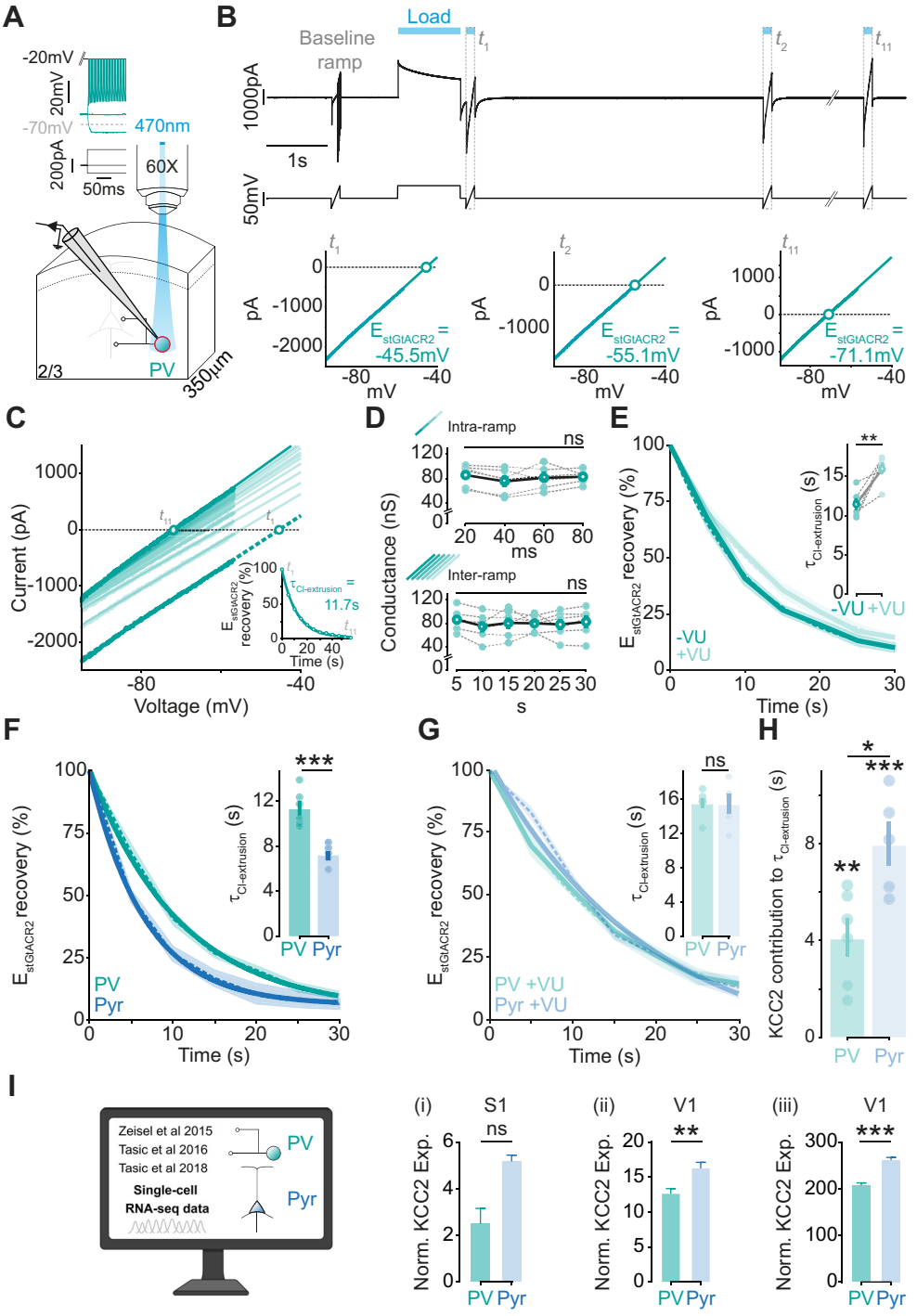


**Figure 6.** Optogenetic $E_{Inh}$ dynamics reveal neuron-specific differences in KCC2-mediated extrusion. ***A***, Whole-cell patch-clamp recordings (pipette solution, 4 mM $Cl^-$) were performed from stGtACR2-expressing L2/3 PV interneurons in the S1. Inset, current-clamp recording from an example stGtACR2-expresssing fast-spiking PV interneuron. ***B***, Voltage-clamp ramp protocol used to monitor $E_{stGtACR2}$ recovery following a stGtACR2-mediated $Cl^-$ load. Example data from a PV interneuron indicate the recorded current (top), estimated holding potential following series resistance correction (middle), and resulting IV plots (bottom) showing the isolated stGtACR2 current at $t_1$, $t_2$, and $t_{11}$. Conventions as in Figure 4. ***C***, IV plot of isolated stGtACR2 currents from $t_1$ to $t_{11}$ in a PV interneuron. Inset, $E_{stGtACR2}$ recovery following $Cl^-$ load. A single exponential fit provides the time constant of $Cl^-$ extrusion ($\tau_{Cl\text{-}extrusion}$). ***D***, The amplitude of the PV interneuron stGtACR2 conductance remained stable within each ramp (top; mean percentage change in conductance across 20 ms periods was $-6.26 \pm 2.98\%$, $p = 0.24$, one-way ANOVA) and across ramps (bottom; $-8.51 \pm 2.42\%$ conductance change at intervals of 5 s, $p = 0.82$, one-way ANOVA), consistent with a modest contribution of desensitization mechanisms ($n = 6$ neurons from 3 mice). ***E***, $E_{stGtACR2}$ recovery in PV interneurons under control conditions (−VU; dark cyan) and when KCC2 was blocked with the selective antagonist VU0463271 (+VU, 10 µM; light cyan). Inset, KCC2 block results in a slowing in $Cl^-$ extrusion in PV interneurons (−VU: $11.38 \pm 0.65$ s vs +VU: $15.57 \pm 0.63$ s, $p = 0.006$, paired $t$ test). ***F***, $E_{stGtACR2}$ recovery following a $Cl^-$ load was slower in PV interneurons than pyramidal neurons. Inset, $Cl^-$ extrusion time constant ($\tau_{Cl\text{-}extrusion}$) was greater in PV interneurons (PV: $11.38 \pm 0.65$ s vs Pyr: $7.29 \pm 0.41$ s, $p = 0.0007$, unpaired $t$ test). Pyramidal neuron data replotted from Figure 4. ***G***, $E_{stGtACR2}$ recovery and the resulting $Cl^-$ extrusion time constant were indistinguishable in PV interneurons and pyramidal neurons after KCC2 block (PV: $15.57 \pm 0.63$ s vs Pyr: $15.79 \pm 0.98$ s, $p = 0.84$, unpaired $t$ test). ***H***, While PV interneurons and pyramidal neurons both exhibited a significant contribution of KCC2 to their $Cl^-$ extrusion time constant (PV: $p = 0.004$, one-sample $t$ test; Pyr: $p = 0.001$, one-sample $t$ test), KCC2's contribution to $Cl^-$ extrusion was significantly less in PV interneurons (PV: $4.13 \pm 0.79$, $n = 6$ neurons from 3 mice vs Pyr: $8.01 \pm 0.92$, $n = 5$ neurons from 3 mice, $p = 0.01$, unpaired $t$ test). ***I***, Meta-analysis of single-cell RNA sequencing data on KCC2 levels in isolated pyramidal neurons and PV interneurons from the sensory cortex. Normalized KCC2 RNA expression levels are lower in PV interneurons than pyramidal neurons in three separate studies: (i) Zeisel et al. (2015) in the S1 (PV: $2.54 \pm 0.62$, $n = 10$

in vitro and in vivo, is shown to capture differences in $E_{Inh}$ dynamics following manipulations of endogenous $Cl^-$ fluxes, and reveals distinct resting $E_{Inh}$ across genetically defined neuronal subpopulations. Furthermore, using our optogenetic approach to challenge $Cl^-$ homeostasis, we quantify a cell's $E_{Inh}$ dynamics and uncover cell-specific $Cl^-$ extrusion processes that are supported by the differential expression of endogenous handling mechanisms.

Our characterization focused on the soma-targeted, anion channel, stGtACR2 (Govorunova et al., 2015; Alfonsa et al., 2016; Mahn et al., 2018). To establish the potential of using stGtACR2 to estimate $E_{Inh}$, $E_{stGtACR2}$ was determined across a range of intracellular $Cl^-$ concentrations (4–70 mM) and compared with estimates of $E_{GABAAR}$. The strong, positive correlation across a population of neurons supported the conclusion that $E_{stGtACR2}$ reflects $E_{Inh}$. This is consistent with evidence that GtACR2 permeability follows the lyotropic series characteristic of other anion channels and suggests a similar relative permeability to $Cl^-$ and $HCO_3^-$ as the $GABA_AR$, although this remains to be tested directly (Bormann et al., 1987; Govorunova et al., 2015; Sineshchekov et al., 2015; Messier et al., 2018). Further validation came from our gramicidin-perforated recordings of resting $E_{stGtACR2}$ and whole-cell recordings of $E_{stGtACR2}$ recovery following a $Cl^-$ load. Our estimated time constant for $E_{stGtACR2}$ recovery in pyramidal neurons (~7.3 s) was close to previous estimates of the time constant for $E_{Cl}$ recovery (~8 s across six separate studies; Thompson et al., 1988; Luhmann and Prince, 1991; Staley and Proctor, 1999; Jin et al., 2005; Deisz et al., 2011; Raimondo et al., 2012) and is a parameter that has been shown to be invariant to the size of $Cl^-$ load (Deisz et al., 2011). Finally, we also confirmed in multiple cell types that both resting $E_{stGtACR2}$ and $E_{stGtACR2}$ recovery are sensitive to manipulations of a $Cl^-$ exporter, KCC2 (Misgeld et al., 1986; Thompson et al., 1988; Jarolimek et al., 1999; DeFazio et al., 2000).

Although we use the term $E_{Inh}$, the reality is that our optogenetic strategy can estimate the reversal potential regardless of whether the net current flowing through stGtACR2 is outward or inward. The strategy will therefore be effective under conditions when ligand-gated anion channels (e.g., $GABA_A$ or glycine receptors) exert either a hyperpolarizing or depolarizing effect relative to the RMP. This is relevant during brain development, when $E_{Cl}$ is often more depolarized, and an optogenetic strategy may be useful in tracking the maturation of inhibitory synaptic systems (Akerman and Cline, 2007; Richards et al., 2010; Kaila et al., 2014; van Rheede et al., 2015). Similarly, relatively depolarized $E_{Cl}$ values have been observed in a variety of pathological states associated with hyperexcitability, meaning that our optogenetic strategy could be useful in investigations of epilepsy and neuropathic pain (Coull et al., 2003; Kaila et al., 2014; Burman et al., 2022).

Estimates of $E_{Inh}$ have traditionally been made by activating endogenous receptors, either by exogenous application of an agonist (e.g., focal delivery or uncaging of GABA) or by stimulating the release of a relevant endogenous agonist (e.g., electrical or optical activation of presynaptic GABA-releasing axons). There are, however, limitations associated with inferring resting and dynamic $E_{Inh}$ from endogenous receptors (e.g., $GABA_ARs$). This includes the fact that repeated agonist delivery can alter the receptor's properties and availability via desensitization mechanisms (Frosch et al., 1992; Jones and Westbrook, 1995; Gravielle, 2018). Meanwhile, when stimulating GABA-releasing axons, presynaptic mechanisms can affect the probability of neurotransmitter release, which could complicate the interpretation of dynamic $E_{Inh}$ measurements and manipulations that affect the presynaptic neurons (Kullmann et al., 2005). Furthermore, although $GABA_ARs$ are thought to contribute to a neuron's $E_{Inh}$ (Karlsson et al., 2011; Yelhekar et al., 2016; Burman et al., 2023), it is difficult to measure their contribution (e.g., by pharmacological blockade) if the $GABA_AR$ is also being used to estimate $E_{Inh}$.

The stGtACR2-based optogenetic approach addresses these potential limitations associated with agonist-based methods, including avoiding the requirement to pharmacologically isolate an endogenous receptor response (Prenosil et al., 2006; Pamenter et al., 2011). Indeed, the optogenetic approach could be used in cases where a cell type lacks ligand-gated anion channels, where delivering an agonist would not be an option. The ability to restrict $Cl^-$ loads to a defined period of light activation distinguishes our approach from techniques that involve the application of a continuous intracellular $Cl^-$ load via a whole-cell patch pipette, for example (Jarolimek et al., 1999). A further advantage is that optogenetic approaches lend themselves to studies in intact preparations. Accordingly, we show that stGtACR2 can be used to determine $E_{Inh}$ in defined neurons of the intact brain, generating the potential for experiments that could combine dynamic $E_{Inh}$ measurements and manipulations of $Cl^-$-regulatory processes in vivo. This application represents an important complement to the use of $Cl^-$ imaging approaches, which can provide information on cytosolic $Cl^-$ concentration in vivo, but do not capture $E_{Inh}$ (Sulis Sato et al., 2017; Boffi et al., 2018; Rahmati et al., 2021).

The GtACR2-based optogenetic approach offers excellent control over the spatial and temporal resolution and amplitude of the evoked anion currents. The spatial resolution is determined in part by GtACR2's localization within the cell of interest and in part by the resolution of the optical system. This is attractive, as $E_{Inh}$ is thought to vary between subcellular compartments (Duebel et al., 2006; Szabadics et al., 2006; Földy et al., 2010; Ellender et al., 2014). One could imagine examining $E_{Inh}$ in dendrites or at the axon initial segment by targeting GtACR2 to the relevant subcellular compartment and/or using more focal light delivery. Light-controlled methods also make it easy to vary the duration and intensity of the anion current, which allows the experimenter to systematically vary $Cl^-$ fluxes over a range of durations (milliseconds to tens of seconds) and amplitudes (via light intensity). This can help to minimize unwanted changes to $E_{Inh}$ caused by sustained endogenous receptor activation (Ehrlich et al., 1999; Akerman and Cline, 2006) while allowing one to control the duration and intensity of $Cl^-$ fluxes in order to quantify $E_{Inh}$ dynamics.

By targeting stGtACR2 to genetically defined cell types, we demonstrated that PV interneurons and pyramidal neurons in L2/3 of the mouse visual cortex differ in their resting $E_{stGtACR2}$. This supports previous evidence of more depolarized $E_{Inh}$ values

←

neurons vs Pyr: 5.23 ± 0.23, $n = 286$ neurons, $p = 0.07$, Kolmogorov–Smirnov test, Dunn's multiple comparison test), (ii) Tasic et al. (2016) in the V1 (PV: 9.73 ± 0.59, $n = 270$ neurons vs Pyr: 16.40 ± 0.71, $n = 756$ neurons, $p = 0.0073$, Kolmogorov–Smirnov test), and (iii) Tasic et al. (2018) in the V1 (PV: 209.5 ± 3.25, $n = 1,337$ neurons vs Pyr: 264.3 ± 2.94, $n = 7,366$ neurons, $p < 0.0001$, Kolmogorov–Smirnov test). *, $p < 0.05$; **, $p < 0.01$; ***, $p < 0.001$.

in interneurons of the mature hippocampus and cortex (Martina et al., 2001; Otsu et al., 2020; Călin et al., 2023). When related to cell-type differences in RMPs, this can generate similar $GABA_AR$ driving forces under resting conditions (Otsu et al., 2020), although there are likely to be differences related to age and the level of network activity (Sauer and Bartos, 2010; Burman et al., 2023). Indeed, such differences in somatic $E_{Inh}$ may underlie cell-type-specific functions. For example, it has been proposed that relatively depolarized $E_{Inh}$ values in PV interneurons may tend to favor shunting inhibition and enable PV interneurons to promote coherent oscillatory network activity (Vida et al., 2006). An interesting future direction will be to use optogenetic approaches to determine $E_{Inh}$ dynamics in different, genetically defined, cell populations.

In terms of the mechanisms that determine a cell's transmembrane gradients, we found that KCC2 makes a similar contribution to resting $E_{Inh}$ in both PV interneurons and pyramidal neurons, supporting recent evidence from the hippocampus (Otsu et al., 2020). This would suggest that KCC2 is not responsible for the different resting $E_{Inh}$ between these two neuron types and that other ion fluxes contribute. The biophysical prediction is that more subtle differences in a cotransporter's activity can be revealed under an ionic load, which might better represent a neuron's state within an active network (Doyon et al., 2016b; Burman et al., 2023). In line with this prediction, we capitalized upon the control of stGtACR2 to both challenge and then monitor $E_{Inh}$ recovery through rapid and sequential measurements. This enabled us to quantify $E_{Inh}$ dynamics and $Cl^-$ extrusion processes in real time, which is difficult with agonist-based approaches (Raimondo et al., 2012). We reveal that PV interneurons exhibit a slower recovery to a transient $Cl^-$ load and that this difference in $E_{Inh}$ dynamics is due to a differential contribution by KCC2, as blocking the cotransporter normalized $E_{Inh}$ dynamics across neurons. This was corroborated by our meta-analysis of single-cell RNA sequencing data from the mouse sensory cortex, which revealed higher KCC2 expression in pyramidal neurons than PV interneurons. We therefore propose that our optogenetic strategy generates sensitive estimates of $E_{Inh}$ dynamics, avoiding issues associated with repeated activation of endogenous $Cl^-$-permeable receptors.

In conclusion, we establish an optogenetic and agonist-independent strategy for probing $E_{Inh}$ in vitro and in vivo, in a manner that is compatible with the targeting of defined cell populations and subcellular compartments. This enabled us to quantify the contribution of endogenous ion fluxes to $E_{Inh}$, to distinguish cell-type differences in resting $E_{Inh}$, and to reveal differences in $E_{Inh}$ dynamics between neuronal subpopulations. More generally, this underscores the fact that optogenetic techniques afford opportunities beyond their principal application of modulating neuronal activity. Our findings therefore help to expand the repertoire of optogenetics and encourage the application of other light-activated ion channels in physiological investigations of transmembrane ion gradients and their associated reversal potentials.

## References


Akerman CJ, Cline HT (2006) Depolarizing GABAergic conductances regulate the balance of excitation to inhibition in the developing retinotectal circuit in vivo. J Neurosci 26:5117–5130.

Akerman CJ, Cline HT (2007) Refining the roles of GABAergic signaling during neural circuit formation. Trends Neurosci 30:382–389.

Alfonsa H, Burman RJ, Brodersen PJN, Newey SE, Mahfooz K, Yamagata T, Panayi MC, Bannerman DM, Vyazovskiy VV, Akerman CJ (2023) Intracellular chloride regulation mediates local sleep pressure in the cortex. Nat Neurosci 26:64–78.

Alfonsa H, Lakey JH, Lightowlers RN, Trevelyan AJ (2016) Cl-out is a novel cooperative optogenetic tool for extruding chloride from neurons. Nat Commun 7:13495.

Alger BE, Nicoll RA (1979) GABA-mediated biphasic inhibitory responses in hippocampus. Nature 281:315–317.

Banke TG, McBain CJ (2006) GABAergic input onto CA3 hippocampal interneurons remains shunting throughout development. J Neurosci 26: 11720–11725.

Berndt A, Lee SY, Ramakrishnan C, Deisseroth K (2014) Structure-guided transformation of channelrhodopsin into a light-activated chloride channel. Science 344:420–424.

Boffi JC, Knabbe J, Kaiser M, Kuner T (2018) KCC2-dependent steady-state intracellular chloride concentration and pH in cortical layer 2/3 neurons of anesthetized and awake mice. Front Cell Neurosci 12:7.

Bormann J, Hamill OP, Sakmann B (1987) Mechanism of anion permeation through channels gated by glycine and gamma-aminobutyric acid in mouse cultured spinal neurones. J Physiol 385:243–286.

Burman RJ, Rosch RE, Wilmshurst JM, Sen A, Ramantani G, Akerman CJ, Raimondo JV (2022) Why won't it stop? The dynamics of benzodiazepine resistance in status epilepticus. Nat Rev Neurol 18:428–441.

Burman RJ, Brodersen PJN, Raimondo JV, Sen A, Akerman CJ (2023) Active cortical networks promote shunting fast synaptic inhibition in vivo. Neuron 111:3531–3540.e6.

Călin A, Waseem T, Raimondo JV, Newey SE, Akerman CJ (2023) A genetically targeted ion sensor reveals distinct seizure-related chloride and pH dynamics in GABAergic interneuron populations. iScience 26: 106363.

Coull JAM, Boudreau D, Bachand K, Prescott SA, Nault F, Sík A, Koninck PD, Koninck YD (2003) Trans-synaptic shift in anion gradient in spinal lamina I neurons as a mechanism of neuropathic pain. Nature 424:938–942.

Cunningham MD, Enna SJ (1996) Evidence for pharmacologically distinct GABAB receptors associated with cAMP production in rat brain. Brain Res 720:220–224.

Currin CB, Trevelyan AJ, Akerman CJ, Raimondo JV (2020) Chloride dynamics alter the input-output properties of neurons. PLoS Comput Biol 16:e1007932.

DeFazio RA, Keros S, Quick MW, Hablitz JJ (2000) Potassium-coupled chloride cotransport controls intracellular chloride in rat neocortical pyramidal neurons. J Neurosci 20:8069–8076.

Deisz RA, Lehmann T-N, Horn P, Dehnicke C, Nitsch R (2011) Components of neuronal chloride transport in rat and human neocortex: neuronal chloride transport in rat and human cortex. J Physiol 589:1317–1347.

Delpire E, Baranczak A, Waterson AG, Kim K, Kett N, Morrison RD, Daniels JS, Weaver CD, Lindsley CW (2012) Further optimization of the K-Cl cotransporter KCC2 antagonist ML077: development of a highly selective and more potent in vitro probe. Bioorg Med Chem Lett 22:4532–4535.

Doyon N, Prescott SA, Castonguay A, Godin AG, Kröger H, Koninck YD (2011) Efficacy of synaptic inhibition depends on multiple, dynamically interacting mechanisms implicated in chloride homeostasis. PLoS Comput Biol 7:e1002149.

Doyon N, Prescott SA, De Koninck Y (2016a) Mild KCC2 hypofunction causes inconspicuous chloride dysregulation that degrades neural coding. Front Cell Neurosci 9:516.

Doyon N, Vinay L, Prescott SA, De Koninck Y (2016b) Chloride regulation: a dynamic equilibrium crucial for synaptic inhibition. Neuron 89:1157–1172.

Duebel J, Haverkamp S, Schleich W, Feng G, Augustine GJ, Kuner T, Euler T (2006) Two-photon imaging reveals somatodendritic chloride gradient in retinal ON-type bipolar cells expressing the biosensor Clomeleon. Neuron 49:81–94.

Düsterwald KM, Currin CB, Burman RJ, Akerman CJ, Kay AR, Raimondo JV (2018) Biophysical models reveal the relative importance of transporter proteins and impermeant anions in chloride homeostasis Swartz KJ, Aldrich R, Jones S, Toombes G, eds. Elife 7:e39575.

Ehrlich I, Löhrke S, Friauf E (1999) Shift from depolarizing to hyperpolarizing glycine action in rat auditory neurones is due to age-dependent $Cl^-$ regulation. J Physiol 520:121–137.

Elkin LA, Kay M, Higgins JJ, Wobbrock JO (2021) An aligned rank transform procedure for multifactor contrast tests. Available at: http://arxiv.org/abs/2102.11824 [Accessed February 6, 2023].

Ellender TJ, Raimondo JV, Irkle A, Lamsa KP, Akerman CJ (2014) Excitatory effects of parvalbumin-expressing interneurons maintain hippocampal epileptiform activity via synchronous afterdischarges. J Neurosci 34: 15208–15222.
Ellender TJ, et al. (2019) Embryonic progenitor pools generate diversity in fine-scale excitatory cortical subnetworks. Nat Commun 10:5224.
Földy C, Lee S-H, Morgan RJ, Soltesz I (2010) Regulation of fast-spiking basket cell synapses by the chloride channel ClC-2. Nat Neurosci 13:1047–1049.
Frosch MP, Lipton SA, Dichter MA (1992) Desensitization of GABA-activated currents and channels in cultured cortical neurons. J Neurosci 12:3042–3053.
Govorunova EG, Sineshchekov OA, Janz R, Liu X, Spudich JL (2015) Natural light-gated anion channels: a family of microbial rhodopsins for advanced optogenetics. Science 349:647–650.
Gravielle MC (2018) Regulation of GABAA receptors by prolonged exposure to endogenous and exogenous ligands. Neurochem Int 118:96–104.
Harden S (2022) pyABF. Available at: https://pypi.org/project/pyabf.
Ilie A, Raimondo JV, Akerman CJ (2012) Adenosine release during seizures attenuates GABAA receptor-mediated depolarization. J Neurosci 32: 5321–5332.
Jarolimek W, Lewen A, Misgeld U (1999) A furosemide-sensitive potassium chloride cotransporter counteracts intracellular chloride accumulation and depletion in cultured rat midbrain neurons. J Neurosci 19: 4695–4704.
Jin X, Huguenard JR, Prince DA (2005) Impaired chloride extrusion in layer V pyramidal neurons of chronically injured epileptogenic neocortex. J Neurophysiol 93:2117–2126.
Jones MV, Westbrook GL (1995) Desensitized states prolong GABAA channel responses to brief agonist pulses. Neuron 15:181–191.
Jouhanneau J-S, Poulet JFA (2019) Multiple two-photon targeted whole-cell patch-clamp recordings from monosynaptically connected neurons in vivo. Front Synaptic Neurosci 11:1.
Kaila K, Voipio J (1987) Postsynaptic fall in intracellular p H induced by GABA-activated bicarbonate conductance. Nature 330:163–165.
Kaila K, Price TJ, Payne JA, Puskarjov M, Voipio J (2014) Cation–chloride cotransporters in neuronal development, plasticity and disease. Nat Rev Neurosci 15:637–654.
Karlsson U, Druzin M, Johansson S (2011) Chloride concentration changes and desensitization of GABAA and glycine receptors. J Gen Physiol 138:609–626.
Kätzel D, Zemelman BV, Buetfering C, Wölfel M, Miesenböck G (2011) The columnar and laminar organization of inhibitory connections to neocortical excitatory cells. Nat Neurosci 14:100–107.
Kirmse K, Kummer M, Kovalchuk Y, Witte OW, Garaschuk O, Holthoff K (2015) GABA depolarizes immature neurons and inhibits network activity in the neonatal neocortex in vivo. Nat Commun 6:7750.
Kitamura K, Judkewitz B, Kano M, Denk W, Häusser M (2008) Targeted patch-clamp recordings and single-cell electroporation of unlabeled neurons in vivo. Nat Methods 5:61–67.
Kullmann DM, Ruiz A, Rusakov DM, Scott R, Semyanov A, Walker MC (2005) Presynaptic, extrasynaptic and axonal GABAA receptors in the CNS: where and why? Prog Biophys Mol Biol 87:33–46.
Kyrozis A, Reichling DB (1995) Perforated-patch recording with gramicidin avoids artifactual changes in intracellular chloride concentration. J Neurosci Methods 57:27–35.
Lanz A, Gordon G, Bains J (2020) Spatiotemporal chloride dynamics in hypothalamic CRHPVN neurons. bioRxiv:1–31.
Luhmann HJ, Prince DA (1991) Postnatal maturation of the GABAergic system in rat neocortex. J Neurophysiol 65:247–263.
Mahn M, Gibor L, Patil P, Malina KC-K, Oring S, Printz Y, Levy R, Lampl I, Yizhar O (2018) High-efficiency optogenetic silencing with soma-targeted anion-conducting channelrhodopsins. Nat Commun 9:4125.
Margrie TW, Brecht M, Sakmann B (2002) In vivo, low-resistance, whole-cell recordings from neurons in the anaesthetized and awake mammalian brain. Pflüg Arch 444:491–498.
Martina M, Royer S, Paré D (2001) Cell-type-specific GABA responses and chloride homeostasis in the cortex and amygdala. J Neurophysiol 86: 2887–2895.
Messier JE, Chen H, Cai Z-L, Xue M (2018) Targeting light-gated chloride channels to neuronal somatodendritic domain reduces their excitatory effect in the axon Raman IM, Westbrook GL, eds. Elife 7:e38506.
Misgeld U, Deisz RA, Dodt HU, Lux HD (1986) The role of chloride transport in postsynaptic inhibition of hippocampal neurons. Science 232:1413–1415.
Otsu Y, Donneger F, Schwartz EJ, Poncer JC (2020) Cation–chloride cotransporters and the polarity of GABA signalling in mouse hippocampal parvalbumin interneurons. J Physiol 598:1865–1880.
Pamenter ME, Hogg DW, Ormond J, Shin DS, Woodin MA, Buck LT (2011) Endogenous GABAA and GABAB receptor-mediated electrical suppression is critical to neuronal anoxia tolerance. Proc Natl Acad Sci U S A 108: 11274–11279.
Payne JA, Rivera C, Voipio J, Kaila K (2003) Cation–chloride co-transporters in neuronal communication, development and trauma. Trends Neurosci 26:199–206.
Prenosil GA, Schneider Gasser EM, Rudolph U, Keist R, Fritschy J-M, Vogt KE (2006) Specific subtypes of GABAA receptors mediate phasic and tonic forms of inhibition in hippocampal pyramidal neurons. J Neurophysiol 96:846–857.
Rahmati N, Normoyle KP, Glykys J, Dzhala VI, Lillis KP, Kahle KT, Raiyyani R, Jacob T, Staley KJ (2021) Unique actions of GABA arising from cytoplasmic chloride microdomains. J Neurosci 41:4957–4975.
Raimondo JV, Kay L, Ellender TE, Akerman CJ (2012) Optogenetic silencing strategies differ in their effects on inhibitory synaptic transmission. Nat Neurosci 15:1102–1104.
Richards BA, Voss OP, Akerman CJ (2010) GABAergic circuits control stimulus-instructed receptive field development in the optic tectum. Nat Neurosci 13:1098–1106.
Rivera C, Voipio J, Payne JA, Ruusuvuori E, Lahtinen H, Lamsa K, Pirvola U, Saarma M, Kaila K (1999) The potassium chloride co-transporter KCC2 renders GABA hyperpolarizing during neuronal maturation. Nature 397:5.
Sauer J-F, Bartos M (2010) Recruitment of early postnatal parvalbumin-positive hippocampal interneurons by GABAergic excitation. J Neurosci 30:110–115.
Sineshchekov OA, Govorunova EG, Li H, Spudich JL (2015) Gating mechanisms of a natural anion channelrhodopsin. Proc Natl Acad Sci U S A 112:14236–14241.
Staley KJ, Mody I (1992) Shunting of excitatory input to dentate gyrus granule cells by a depolarizing GABAA receptor-mediated postsynaptic conductance. J Neurophysiol 68:197–212.
Staley KJ, Proctor WR (1999) Modulation of mammalian dendritic GABA-a receptor function by the kinetics of chloride and bicarbonate transport. J Physiol 519:693–712.
Sulis Sato S, et al. (2017) Simultaneous two-photon imaging of intracellular chloride concentration and pH in mouse pyramidal neurons in vivo. Proc Natl Acad Sci U S A 114:E8770–E8779.
Szabadics J, Varga C, Molnár G, Oláh S, Barzó P, Tamás G (2006) Excitatory effect of GABAergic axo-axonic cells in cortical microcircuits. Science 311:233–235.
Tabata H, Nakajima K (2001) Efficient in utero gene transfer system to the developing mouse brain using electroporation: visualization of neuronal migration in the developing cortex. Neuroscience 103:865–872.
Takeuchi A, Takeuchi N (1967) Anion permeability of the inhibitory postsynaptic membrane of the crayfish neuromuscular junction. J Physiol 191:575–590.
Tasic B, et al. (2016) Adult mouse cortical cell taxonomy revealed by single cell transcriptomics. Nat Neurosci 19:335–346.
Tasic B, et al. (2018) Shared and distinct transcriptomic cell types across neocortical areas. Nature 563:72–78.
Thompson SM, Deisz RA, Prince DA (1988) Relative contributions of passive equilibrium and active transport to the distribution of chloride in mammalian cortical neurons. J Neurophysiol 60:105–124.
Traynelis SF (1998) Software-based correction of single compartment series resistance errors. J Neurosci Methods 86:25–34.
van Rheede JJ, Richards BA, Akerman CJ (2015) Sensory-evoked spiking behavior emerges via an experience-dependent plasticity mechanism. Neuron 87:1050–1062.
Verheugen JA, Fricker D, Miles R (1999) Noninvasive measurements of the membrane potential and GABAergic action in hippocampal interneurons. J Neurosci 19:2546–2555.
Vida I, Bartos M, Jonas P (2006) Shunting inhibition improves robustness of gamma oscillations in hippocampal interneuron networks by homogenizing firing rates. Neuron 49:107–117.

Wang Y, Liu Y, Wang S, Wang Z (2016) In vivo whole-cell recording with high success rate in anaesthetized and awake mammalian brains. Mol Brain 9:86.

Wiegert JS, Mahn M, Prigge M, Printz Y, Yizhar O (2017) Silencing neurons: tools, applications, and experimental constraints. Neuron 95:504–529.

Wietek J, Wiegert JS, Adeishvili N, Schneider F, Watanabe H, Tsunoda SP, Vogt A, Elstner M, Oertner TG, Hegemann P (2014) Conversion of channelrhodopsin into a light-gated chloride channel. Science 344:409–412.

Wobbrock JO, Findlater L, Gergle D, Higgins JJ (2011) The aligned rank transform for nonparametric factorial analyses using only anova procedures. Proceedings of the SIGCHI Conference on Human Factors in Computing Systems 143–146.

Yelhekar TD, Druzin M, Karlsson U, Blomqvist E, Johansson S (2016) How to properly measure a current-voltage relation?—Interpolation vs ramp methods applied to studies of GABAA receptors. Front Cell Neurosci 10:10.

Yelhekar TD, Druzin M, Johansson S (2017) Contribution of resting conductance, GABAA-receptor mediated miniature synaptic currents and neurosteroid to chloride homeostasis in central neurons. eNeuro 4:9–17.

Zeisel A, et al. (2015) Cell types in the mouse cortex and hippocampus revealed by single-cell RNA-seq. Science 347:1138–1142.

Zhao S, et al. (2011) Cell type–specific channelrhodopsin-2 transgenic mice for optogenetic dissection of neural circuitry function. Nat Methods 8: 745–752.